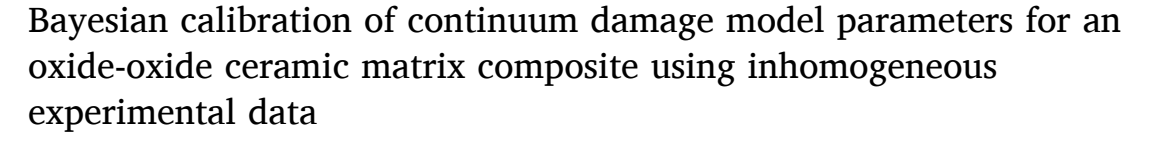
Contents lists available at ScienceDirect

# Mechanics of Materials

journal homepage: www.elsevier.com/locate/mechmat



## **Editor Invited Article**



Adam P. Generale <sup>a</sup>, Richard B. Hall <sup>d</sup>, Robert A. Brockman <sup>e</sup>, V. Roshan Joseph <sup>c</sup>, George Jefferson <sup>d</sup>, Larry Zawada <sup>d,f</sup>, Jennifer Pierce <sup>d,e</sup>, Surya R. Kalidindi <sup>a,b,\*</sup>

- <sup>a</sup> Georgia Institute of Technology, George W. Woodruff School of Mechanical Engineering, Atlanta, GA 30332, USA
- <sup>b</sup> Georgia Institute of Technology, School of Computational Science Engineering, Atlanta, GA 30332, USA
- Georgia Institute of Technology, H. Milton Stewart School of Industrial and Systems Engineering, Atlanta, GA 30332, USA
- <sup>d</sup> Air Force Research Laboratory, Wright-Patterson AFB, OH 45433, USA
- <sup>e</sup> University of Dayton Research Institute, Dayton, OH 45469, USA
- f ARCTOS Technology Solutions, Beavercreek, OH 45432, USA

#### ARTICLE INFO

#### Keywords. Ceramic Matrix Composites Bayesian Inference Markov Chain Monte Carlo Probabilistic Calibration Uncertainty Quantification

# ABSTRACT

The calibration of continuum damage mechanics (CDM) models is often performed by least-squares regression through the design of specifically crafted experiments to identify a deterministic solution of model parameters minimizing the squared error between the model prediction and the corresponding experimental result. Specifically, this work demonstrates a successful application of Bayesian inference for the simultaneous estimation of eleven material parameters of a viscous multimode CDM model conditioned upon a small inhomogeneous multiaxial experimental dataset. The stochastic treatment of CDM model parameters provides uncertainty estimates, enables the propagation of uncertainty into further analyses, and provides for principled decision making regarding informative subsequent experimental tests of value. The methodology presented in this work is also broadly applicable to various mechanical models with high-dimensional parameter sets.

### 1. Introduction

Continuum damage mechanics (CDM) is a branch of continuum mechanics used to describe inelastic damage and fracture processes within materials ranging from initiation through to ultimate fracture (Kachanov, 1986; Lemaitre, 1992; Murakami, 2012). This theory provides computational tractability in modeling the accumulation of damage in a continuum sense rather than the consideration of discrete cracks, and as such, has been widely applied to a variety of material classes (Chaboche, 1993; Lemaitre, 1984; Lemaitre and Chaboche, 1990; Pailhes et al., 2002; Simo and Ju, 1987). In order to correctly capture interdependencies between the different possible damage modes and their respective evolutions, CDM models often employ a large number of model parameters that need to be calibrated to experimental data. The number of model parameters is especially high for materials exhibiting

strong anisotropy prior to damage, such as ceramic-matrix composites (CMCs). This is clearly evident from the many CDM models developed specifically for such materials (Chaboche et al., 1998; Matzenmiller et al., 1995; Oliver, 1989; Pailhes et al., 2002). Traditionally, model calibration is often accomplished through least-squares regression of model predictions with corresponding experimental measurements (Mahnken, 2017). Specific experiments are often designed to simplify this calibration process. For example, Camus (2000) calibrated the parameters in their CDM model by matching the model predictions for the stress-strain responses in both on- and off-axis (0° and 45°, respectively) uniaxial loading with the corresponding measurements. A similar methodology was also used by Chaboche and Maire (2002) and Pailhes et al. (2002). Although this simple approach ensures that the model predictions match closely with the experimental data in the specific tests used in the calibration process, they do not guarantee good predictions

<sup>\*</sup> Corresponding author. Georgia Institute of Technology, George W. Woodruff School of Mechanical Engineering, Atlanta, GA 30332, USA. E-mail addresses: agenerale3@gatech.edu (A.P. Generale), richard.hall.16@us.af.mil (R.B. Hall), Robert.Brockman@udri.udayton.edu (R.A. Brockman), roshan@ gatech.edu (V.R. Joseph), george.jefferson.1@us.af.mil (G. Jefferson), Jennifer.Pierce@udri.udayton.edu (J. Pierce), surya.kalidindi@me.gatech.edu



0167-6636/© 2022 Elsevier Ltd. All rights reserved.

Available online 7 October 2022

(S.R. Kalidindi).

Received 30 June 2022; Received in revised form 27 September 2022; Accepted 3 October 2022



for other loading conditions. Furthermore, these approaches do not allow for a proper treatment of the stochasticity inherent in the measurements. There are indeed many sources of uncertainty in both the physical experiments and the numerical models that need to be taken into account in the model calibration process. These may include the many simplifications/idealizations introduced into the CDM model as well as the accuracy/resolution limits for the experimental data.

Bayesian inference (Adeli et al., 2020; Knipprath, 2010) offers novel avenues for the calibration of the CDM models to available experimental data. In this approach, one not only treats the measurements as stochastic outcomes of experiments, but also treats the model parameters as random variables. Therefore, it is assumed that any individual experimental observation can only help reduce the uncertainty in the distribution of the model parameter sets. Some of the inherent advantages of this approach are that it allows for the consideration of a wide variety of experimental observations (from different test protocols) and accounts for any inherent correlations among the model parameters. The latter is especially important for over-parameterized models with limited observations (Van Oijen et al., 2005), similar to the conditions encountered in the calibration of CDM models for CMCs. Bayesian inference has been successfully applied in simpler problems such as the identification of elastic constants in an aluminum alloy (Pacheo et al., 2016), a polymeric material embedded in glass (Zhang et al., 2012), as well as on laminate composites (Castillo and Kalidindi, 2019; Gallina et al., 2015). They are being increasingly explored for the calibration of the more sophisticated material constitutive models such as the one-dimensional Von-Mises plasticity model with strain hardening (Mahnken, 2017), viscoelasticity (Mehrez et al., 2015; Miles et al., 2015; Zhang et al., 2013), viscoplasticity (Adeli and Matthies, 2019), and viscous-damage models (Adeli et al., 2020; Ding et al., 2020). It should be noted that the total number of calibrated model parameters in these prior studies were fewer than five, and the calibration was performed on small homogeneous datasets. These approaches have not yet been extended to models with larger numbers of model parameters, largely due to the relative scarcity of suitable experimental data. Indeed, the broader application of these methods is only practically feasible if one aggregates and uses inhomogeneous data (e.g., experimental observations in distinct multiaxial loading conditions) in the calibration process. The use of inhomogeneous data is also very likely to sharply improve the accuracy and robustness of the estimated distributions on the model parameters.

In this work, Bayesian inference is applied in the probabilistic calibration of a total of eleven elastic and inelastic damage parameters of a viscous multimode damage model developed by Hall and Brockman (Hall et al., 2021, 2022; Hall and Brockman, 2020, 2021). The experimental dataset used for this calibration was taken from prior efforts at Air Force Research Laboratory (Jefferson et al., 2018)<sup>1</sup>. It consisted of two uniaxial and five multiaxial (tension-torsion) tests, each with distinct loading ratios and rates (there are no duplicate tests in the dataset). The material evaluated in these tests was an oxide/oxide, Nextel™ 720/AS CMC, arranged in 8-harness satin plies woven into thin-walled tubular specimens with an involute ply lay-up. The CDM model is defined through an Abaqus user-defined material model (UMAT) (Dassault, 2019), and is compiled as an external library within the Bayesian calibration framework. The modular approach described in this work is broadly applicable to a wide variety of custom material constitutive models that can be implemented as user-subroutines within commercial FE solvers.

### 2. Methods

The CMC viscous deformation and damage model considered in this

work is taken from the work of Hall and Brockman (Hall et al., 2021, 2022; Hall and Brockman, 2020, 2021). One key aspect of CMCs which allows for their operation in extreme (thermal) environments is its damage tolerant behavior, facilitated by an internal fibrous structure (Bansal and Lamon, 2014) that is key to avoiding the catastrophic failure observed commonly in monolithic ceramics. Under monotonically increasing load, the CMC exhibits various energy dissipating damage mechanisms such as matrix cracking, interface debonding, sliding at the fiber matrix interface, and fiber fracture. These microstructural damage mechanisms occur over a distributed region allowing for flaw insensitivity and overall nonlinear behavior (Kumar et al., 2019). Increased utilization of CMCs in structural applications requires a method for mathematically modeling its behavior at component length scales, lumping together these varied energy dissipating damage mechanisms. CDM provides one such avenue, and has effectively been used in the modeling of such materials under varied loading conditions (Camus, 2000; Chaboche et al., 1998; Chaboche and Maire, 2002; Pailhes et al., 2002).

## 2.1. Viscous multimode damage model

An overview of the multimode damage model considered in this work is presented here briefly. A more thorough treatment of the mathematical foundations can be seen in the works of Hall and Brockman (Hall et al., 2021; Hall and Brockman, 2020, 2021). In this model, damage is described as a fourth-order tensor exhibiting orthotropic symmetry (with nine independent components). The isothermal state in the principal material frame is defined by the following list of variables:

$$s = \{E_i, D_\alpha, w_\alpha\}$$
  $i = 1, 2, ..., 6;$   $\alpha = 1, 2, ..., 9$  (1)

where  $E_i$  denote the (vectorized) components of the Green strain measure,  $D_\alpha$  are the independent components (referred here as damage modes) of the orthotropic damage tensor, and  $w_\alpha$  are indirect measures of work associated with  $D_\alpha$ . Specifically,

$$\begin{aligned} [E] &= \begin{bmatrix} E_{11} & E_{22} & E_{33} & 2E_{23} & 2E_{31} & 2E_{12} \end{bmatrix}^{T} \\ [D] &= \begin{bmatrix} D_{1} & D_{2} & D_{3} & D_{4} & D_{5} & D_{6} & D_{7} & D_{8} & D_{9} \end{bmatrix}^{T} \\ &= \begin{bmatrix} D_{1111} & D_{2222} & D_{3333} & 4D_{2323} & 4D_{1313} & 4D_{1212} & 2D_{2233} & 2D_{1133} & 2D_{1122} \end{bmatrix}^{T} \end{aligned}$$

$$(22)$$

 $w_a$  are related to the threshold values of damage energy release rates on the  $\alpha$  planes,  $y_\alpha$ , as (no implied summation on the Greek indices)

$$w_{\alpha} = \int_{0}^{t} \dot{w}_{\alpha} dt, \dot{w}_{\alpha} = y_{\alpha}[w_{\alpha}] \dot{D}_{\alpha}, y_{\alpha}[w_{\alpha}] = y_{\alpha}^{0} + \int_{0}^{t} c_{\alpha} y_{\alpha}[w_{\alpha}[\xi]] \dot{D}_{\alpha}[\xi] d\xi$$
 (3)

where  $c_{\alpha}$  are material constants related to the expansion of the damage surface in the space of energy release rates, and  $y_{\alpha}^{0}$  is the initial threshold value in the absence of damage.

The model presented above assumes small strains with finite rotations. A co-rotational coordinate system is adopted which rotates according to the rotation component, R, defined in the polar decomposition of the deformation gradient, F. In the relations below, D is the corresponding Green-Nagdhi or Dienes co-rotational rate of the damage tensor, D (Belytschko et al., 2014), and  $L^e$  is defined as the elastic stiffness tensor. It is assumed that the second Piola-Kirchhoff stress, S, satisfies the hyperelastic relation with the Helmholtz energy,

$$S = \rho_0 \frac{\partial \psi[s]}{\partial E}, \psi = \frac{1}{2}E : L^e[D] : E$$
(4)

The rate of dissipation is then given by

$$Y: \overset{\Delta}{D} - \rho_0 \sum_{\alpha=1}^{9} \frac{\partial \psi}{\partial w_{\alpha}} \dot{w}_{\alpha} \ge 0 \tag{5}$$

<sup>&</sup>lt;sup>1</sup> These tests were a continuation of efforts initiated in partnership with the Air Force Institute of Technology (DeRienzo, 2013; Hilburn, 2014), using the same specimen material and involute tubular geometry.

where the damage energy release rate Y is defined as

$$Y = -\rho_0 \partial \psi[s]/\partial D \tag{6}$$

Consistent with the vectorized representations introduced earlier, a compact representation for Y is introduced as

$$[Y] = [Y_{1111} \quad Y_{2222} \quad Y_{3333} \quad Y_{2323} \quad Y_{1313} \quad Y_{1212} \quad Y_{2233} \quad Y_{1133} \quad Y_{1122}]^T$$
 (7)

The second law is then enforced in the modified sense below, where  $\zeta$  is the corresponding modal dissipation function:

$$\sum_{a}^{9} \left( F_{a} \overset{\Delta}{D}_{a} - \rho_{0} \frac{\partial \psi}{\partial w_{a}} \dot{w}_{a} \right) = \zeta \left[ \overset{\Delta}{D}_{a}, \dot{w}_{a}; s \right] \ge 0 \tag{8}$$

$$F_{a} = Y_{a} (f_{a})^{q_{a}}, \quad f_{a} = \left( \frac{\sum_{\beta}^{9} \mathbf{H}_{a\beta}^{-1} Y_{\beta}}{Y_{a} [w_{a}]} - 1 \right)$$
 (9)

where  $\langle \bullet \rangle$  is the Heaviside function,  $\beta = 1, 2, ..., 9$ , and the  $\mathbf{H}^{-1}$  matrix has diagonal entries  $1/H_{aa}$  and off-diagonal entries  $-n_{a\beta}/H_{aa}$ .

The assumption of maximum dissipation rate (Hall et al., 2021; Rajagopal and Srinivasa, 1998, 2004) leads to

$$\overset{\Delta}{D}_{\beta} = \sum_{\alpha}^{9} \boldsymbol{H}_{\beta\alpha}^{-1}[s] Y_{\alpha}(f_{\alpha})^{q_{\alpha}} \equiv \sum_{\alpha}^{9} \boldsymbol{H}_{\beta\alpha}^{-1}[s] F_{\alpha}$$
(10)

where the same matrix  $\mathbf{H}^{-1}$  is assumed in Equations (9) and (10) for simplicity.

In the present tension-torsion application, only damages modes 1 and 6 are active, such that damage evolution is defined as

$$\hat{D}_{1} = \frac{1}{H_{11}} Y_{1}(f_{1})^{q_{1}} - \frac{n_{16}}{H_{11}} Y_{6}(f_{6})^{q_{6}}$$

$$= \frac{1}{H_{11}} Y_{1} \left\langle \frac{(Y_{1} - n_{16}Y_{6})/H_{11}}{y_{1}[w_{1}]} - 1 \right\rangle^{q_{1}} - \frac{n_{16}}{H_{11}} Y_{6} \left\langle \frac{Y_{6}/H_{66}}{y_{6}[w_{6}]} - 1 \right\rangle^{q_{6}}$$

$$\hat{D}_{6} = \frac{1}{H_{66}} Y_{6} \left\langle f_{6} \right\rangle^{q_{6}} - \frac{n_{16}}{H_{11}} Y_{1} \left\langle f_{1} \right\rangle^{q_{1}}$$

$$= \frac{1}{H_{66}} Y_{6} \left\langle \frac{Y_{6}/H_{66}}{y_{6}[w_{6}]} - 1 \right\rangle^{q_{6}} - \frac{n_{16}}{H_{11}} Y_{1} \left\langle \frac{(Y_{1} - n_{16}Y_{6})/H_{11}}{y_{1}[w_{1}]} - 1 \right\rangle^{q_{1}}$$
(11)

The directional damage coupling coefficients,  $n_{\alpha\beta}$ , reflect the effects of coupled damage accumulation in normal and shear loadings. At the microstructural level, these coupling parameters reflect the effect of normal stresses on frictional shear deformation occurring at longitudinal crack faces and fiber-matrix interfaces.

## 2.2. Bayesian inference of model parameters

The procedure for estimating model parameters given noisy data is formally known as the inverse problem (Kirsch, 2011; Wu et al., 2018), or model calibration in statistical literature (Box and Hunter, 1962; Kennedy and O'Hagan, 2001). Traditionally such a model is defined as

$$y^E = y^M(\boldsymbol{\theta}) + \xi \tag{12}$$

where  $y^E$  denotes the noisy structured observational data,  $y^M$  the predictive model with unknown parameters  $\theta$ , and  $\xi$  the unknown observational noise. Directly calculating the inverse of the predictive model is generally intractable in practice, limiting methods for the identification of  $\theta$  which best match the experimental data.

The multimode damage model in this work is sufficiently flexible to model wide ranging nonlinear material behavior, at the cost of increased parameterization in its underlying form. This increased parameterization presents challenges in the identification of  $\boldsymbol{\theta}$  when provided with limited or inhomogeneous experimental datasets corrupted by unknown noise and nonlinear effects. It is precisely in this scenario in which Bayesian approaches become increasingly useful, as they treat model parameters as stochastic variables exhibiting a distribution of possible

values, rather than providing a deterministic result. An important property of Bayesian inference is its ability to update one's beliefs, or condition the probability distribution of stochastic variables, as additional data (e.g., experimental observations) becomes available. Given the model form of Eq. (12), Bayes' theorem is commonly expressed as

$$P(\boldsymbol{\theta}|\boldsymbol{y}^{E}) = \frac{P(\boldsymbol{y}^{E}|\boldsymbol{\theta})P(\boldsymbol{\theta})}{P(\boldsymbol{y}^{E})}$$
(13)

where  $P(\theta)$  represents the prior belief on the unknown model parameters  $\theta$ ,  $P(y^E|\theta)$  the likelihood of sampling the observations  $y^E$  for a specific set of model parameters,  $P(y^E)$  is the probability of the evidence, and  $P(\theta|y^E)$  the posterior representing the updated belief on the model parameters  $\theta$  given the observations  $y^E$ . The manipulation of conditional probabilities in Eq. (13) is especially useful in cases where  $P(y^E|\theta)$  is easy to compute, but not  $P(\theta|y^E)$ . The likelihood is often considered to be Gaussian as it arises from the model in Eq. (12) with an assumption of normally distributed white noise. In applications where little prior knowledge over the material model parameters is available, a uniform distribution is often taken for the prior so that its influence over the posterior is limited.

### 2.2.1. Affine-Invariant Ensemble Markov Chain Monte Carlo algorithm

The identification of the multidimensional parameter distribution conditioned on the observed experimental data (i.e., posterior distribution defined in Eq. (13)) was estimated through the Affine-Invariant Ensemble Markov Chain Monte Carlo (MCMC) algorithm (Foreman-Mackey et al., 2013; Goodman and Weare, 2010). This ensemble sampler was utilized primarily for its ability to readily identify skewed or multimodal distributions, both of which were expected in the sampling of such a high dimensional parameter space. The general goal of MCMC algorithms is to draw samples from the posterior probability density as defined in the numerator of Eq. (13). This strategy allows one to sample from the posterior distribution without computing the evidence, which is generally expensive to compute (Foreman-Mackey et al., 2013). The sampling strategy can be viewed as a procedure for generating a random walk in parameter space that given sufficient time, draws a representative set of samples from the posterior distribution. During this random walk, each individual point in the Markov chain  $X(t_i) = \theta_i$ depends solely on the position of the prior step  $X(t_{i-1}) = \theta_{i-1}$ .

In comparison to the standard Metropolis-Hastings (M - H) algorithm, the Affine-Invariant Ensemble algorithm requires the existence of an ensemble of K walkers  $S = \{X_k\}$ , where the proposal distribution for one of the walkers (indexed by k) is based on the locations in parameter space of the remaining K-1 walkers defining the complementary set of walkers  $S_{[k]} = \{X_j, \, \forall j \neq k\}$ . During each iteration, the position of all walkers in the ensemble is updated. In order to update the position of a single walker at position  $X_k$ , a walker is drawn at random from the complementary set  $S_{[k]}$  and the new proposed position for the walker  $X_k$  can be written as

$$W = X_j + Z(X_k(t) - X_j)$$
(14)

with Z being a random variable drawn from the distribution g(z). The particular distribution recommended by Goodman and Weare (2010) is

$$g(z) \propto \begin{cases} \frac{1}{\sqrt{Z}} & \text{if } z \in \left[\frac{1}{a}, a\right] \\ 0 & \text{else} \end{cases}$$
 (15)

where a is a tunable parameter set to 2. The proposal walker location is then accepted with probability

$$q = \min\left(1, Z^{D-1} \frac{P(\mathbf{W})}{P(\mathbf{X}_k(t))}\right)$$
 (16)

where D is the dimensionality of the space being sampled. The proposal is then accepted or rejected when compared against a sample drawn from a standard uniform distribution  $r\leftarrow R \sim U[0,1]$ . If  $r\leq q$  then the transition is accepted and  $X_k(t+1)$  is assigned the position W.

The algorithm described above has been extensively used in astrophysics applications (Chontos et al., 2021; Huang et al., 2021; Suárez Mascareño et al., 2021) where models exhibit similar high-dimensionality as the CDM model considered in this work. In such high-dimensional spaces, traditional algorithms require multiple tunable parameters (their number scaling with the problem size), whereas the Affine-Invariant Ensemble Sampler employs only one parameter (Foreman-Mackey et al., 2013). It has also been shown to provide improved performance in highly skewed distributions (such as the Rosenbrock density) over the conventional M - H algorithm (Goodman and Weare, 2010). The specific MCMC algorithm used in this study is implemented in the Python package emcee, developed by Foreman-Mackey et al. (2013). In practice, the initialization of the ensemble walker positions is recommended to be placed in a tight cluster surrounding an estimate of the maximum likelihood estimate (MLE).

## 2.2.2. Autocorrelation analysis and chain convergence

An ever-present challenge in MCMC sampling is judging when sufficient samples have been drawn to ensure some representative and stationary posterior probability density function (PDF). Unfortunately without having definitive bounds on the smoothness and support of the posterior PDF, it is never truly possible to know that the entire posterior PDF has been correctly sampled (Hogg and Foreman-Mackey, 2018). In real world applications of MCMC sampling, one must rely on heuristics to cease sampling. Examples of these include, observing that each walker has traversed high-probability portions of the parameter space many times, observing trace plots for each parameter to ensure stationary behavior, or observing convergence of the posterior with varied initialization. These heuristics can be made more precise through a quantification of the amount of deviation observed between two subsets of a sampled chain. A metric that formalizes this notion is the integrated autocorrelation time of a chain, of which estimates are foundational in multiple other diagnostic heuristics often employed convergence analysis (Roy, 2019).

As previously discussed MCMC sampling approximates intractable integrals through a Monte Carlo approximation in scenarios where point estimates of  $P(y^E|\theta)$  can be readily obtained without knowledge of its analytical form. The error associated with this approximation is proportional to  $\sqrt{\tau/N}$ , where  $\tau$  is the integrated autocorrelation time, and N the total number of samples (Hogg and Foreman-Mackey, 2018). The autocorrelation time then defines the average time required for the samples to become uncorrelated, and provides a method to calculate the relative error on the target integral (Hogg and Foreman-Mackey, 2018). It is defined as

$$\tau = \sum_{t=-\infty}^{\infty} A(t) = 1 + 2\sum_{t=1}^{\infty} A(t) = 1 + 2\sum_{t=1}^{\infty} \frac{C(t)}{C(0)}$$
(17)

where A(t) is the normalized autocorrelation function of the stochastic process that generated the chain and C(t) is the autocovariance function that measures the amount of correlation between samples separated by an integer lag t. The autocovariance function is defined as

$$C(t) = E_{i}[(X(t_{i}) - \overline{X})(X(t_{i+t}) - \overline{X})] = \lim_{N \to \infty} \frac{1}{N} \sum_{i=1}^{N} (X(t_{i}) - \overline{X})(X(t_{i+t}) - \overline{X})$$
 (18)

where  $\overline{X}$  is the mean. In practice it is not possible to compute the integrated autocorrelation time as it requires an infinitely long chain of samples. It can instead be estimated using a finite chain  $\{X(t_n)\}_{n=1}^N$  as

$$\widehat{C}(t) = \frac{1}{N-t} \sum_{i=1}^{N-t} (X(t_i) - \overline{X})(X(t_{i+t}) - \overline{X})$$
(19)

and this estimate is then propagated through Eq. (17) to obtain an estimate for the autocorrelation time. In practice, it is recommended to use a value  $M \ll N$  as the introduction of this smaller value reduces the variance of the estimator at the cost of a small amount of added bias. Sokal (1996) recommends selecting the value of M such that  $M \ge 5\hat{\tau}(M)$ , and notes that this selection performs well for chains longer than  $1000\hat{\tau}$ . Fortunately, the Affine-Invariant MCMC algorithm contains large numbers of parallel chains of walkers which can be leveraged such that often only chains of length  $50\hat{\tau}$  are required (Foreman-Mackey, 2021).

#### 3. Multiaxial experimental dataset

The experimental dataset used for probabilistic calibration in this work consists of experiments performed at Air Force Research Laboratory (Jefferson et al., 2018). The material evaluated was an oxide/oxide, Nextel<sup>TM</sup> 720/AS CMC, arranged in 8-harness satin plies woven into thin-walled tubular specimens with an involute ply lay-up. The tubes were designed to nominally have an outer diameter of 41 mm with an 85 mm gage length. The involute layup process results in material ply orientation inclines approximately 7° from the hoop direction. In this work, this small angle is neglected and the stresses and strains are reported in the cylindrical coordinate system. Further information regarding the test apparatus, specimen shape, and manufacturing methodology can be found in the theses of Hilburn (2014), DeRienzo (2013) and work by Pagano and Whitford (1985). Relevant details of each test sample considered in this work are summarized in Table 1, where load control information is presented alongside the calculated resulting mean strain rates. All tests were performed under ambient conditions. Of the seven tests performed, one isolated the response in pure tension and one in pure torsion, while the remaining samples were performed at four varying loading ratios and three varied rates.

The measured stress-strain responses are shown in Fig. 1, where it can be observed that the strain to failure varies significantly between samples according to their test parameters. The viscous effects of damage evolution are also evident in the varied stiffness degradation and ultimate strengths at failure.

# 4. Simultaneous Bayesian calibration of damage model

The viscous multimode damage model was simultaneously calibrated against the tension-torsion dataset described in Section 3. This inverse problem of identifying model parameters given the multiaxial tension-torsion dataset was approached through the identification of the active model parameters, namely, elastic constants  $E_1$  and  $G_{12}$ , strength in tension and torsion ( $X_{T1}$  and  $X_{T6}$ ), viscous scaling parameter ( $c_1$  and  $c_6$ ), damage evolution power law exponent ( $q_1$  and  $q_6$ ), damage evolution scaling parameter ( $H_{11}$  and  $H_{66}$ ), and damage coupling parameter  $n_{16}$ . These 11 model parameters are then grouped into the model parameter vector  $\theta$ .

In order to incorporate the experimental curves into the numerical

**Table 1**Experimental data and testing conditions for each thin-walled tubular sample, including loading rates in tension and torsion and the load ratio.

Sample	Axial Rate (MPa/s)	Torsional Rate (MPa/s)		
115	1.000	0.250		
117	0.000	0.400		
119	4.000	0.000		
120	4.000	0.290		
121	0.200	0.014		
122	0.200	0.067		
123	0.200	0.133		

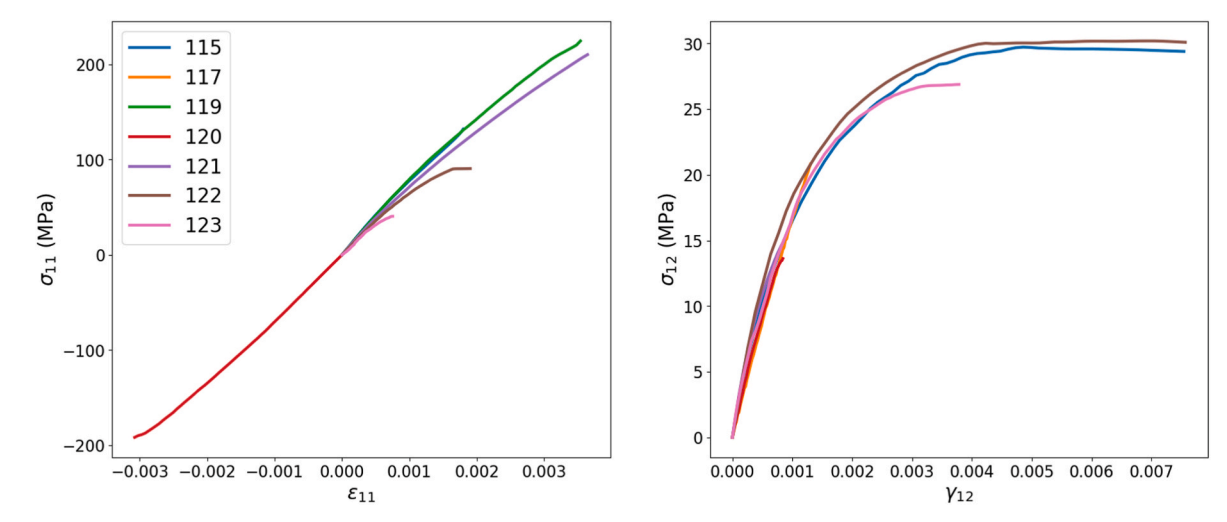


Fig. 1. Measured stress-strain responses in tension-torsion tests for all samples considered in this work.

workflow, each curve in tension and torsion tests was sampled at L evenly spaced points. The stress values in vectorized form were then stacked and grouped into a vector defined as  $s^E$ . The resulting final vector was of the form

$$\mathbf{s}^{E} = \begin{bmatrix} \mathbf{s}_{a1}^{T} & \mathbf{s}_{t1}^{T} & \cdots & \mathbf{s}_{a7}^{T} & \mathbf{s}_{t7}^{T} \end{bmatrix}^{T}$$

$$(20)$$

where  $s_{a1}$  is the vector consisting of all the stress components  $\sigma_{11}$  (at the L evenly spaced strain points) for the first sample, and  $s_{t1}$  the vector consisting of all the shear stress components  $\sigma_{12}$ . Accordingly, the final length of  $s^E$  is 14L. A similar vector could be established for the model output through evaluating the material model at the same strain and time increments as those used for each experimental sample, and populating the vector with stress values from a discretized curve. This was accomplished through direct calls to a driver subroutine wrapped around the Abaqus UMAT subroutine as an externally loaded library. The Abagus UMAT subroutine is used directly for performing stress evaluations. This approach allows the fully three-dimensional model to be used for property identification, while accommodating a mixture of test types with differing stress boundary conditions. The UMAT works with three-dimensional stress and strain states, while the property evaluation process prescribes only the strain quantities relevant to the test data being used for fitting. A wrapper function is provided to perform a Newton-Raphson solution for unspecified strains that correspond to zero stress components, by calling the UMAT multiple times at a single strain sampling point. Robust initializing values are always available from previous time points, ensuring rapid convergence of subsequent iterations. Specific to this application, this driver subroutine identifies strain increments corresponding to the thin-walled planestress condition during tension-torsion testing.

## 4.1. Mixed effects statistical model

The classical definition of the inverse problem described in Section 2.2 for scalar, functional, or tensor output for a singular individual in a population can be extended through the use of mixed effects models (Davidian and Giltinan, 1993, 2003; Pinheiro et al., 2007). Mixed effects models provide a method of handling data in the form of continuous, repeated measurements taken on a number of individuals, such as in the present case of stress-strain responses for a collection of samples, with repeated stress values evolving during progressive loading. Specifically, such models add stochastic terms to account for intra-individual variability (in our case variability across all strain levels in a single test). Importantly, as in the present application these additional stochastic terms will remain constant for a given individual sample, it was

anticipated that the additional model flexibility would aid in accounting for variability in the anisotropy of distinct samples used in the different tests (see Fig. 1). Variability in the experimental response curves of the inhomogeneous dataset naturally lends itself to this statistical description given the impossibility of isolating the contribution of response variation associated with viscous loading effects, or inherent variability in the microstructure of each sample and associated anisotropic response. Minimal variability is expected with test sample preparation and load control during testing. These multiple effects can be captured in the model by introducing a multiplicative random effect  $\beta_i \sim N(1, \sigma_{\beta}^2)$ , for each test i as

$$s_{ii}^{E} = \beta_{i} s_{ii}^{M}(\boldsymbol{\theta}) + \xi_{ii}$$
 (21)

where  $\xi_{ij} \sim N(0,\sigma_{\xi}^2), i=1,...,K$ , with K being the number of tests, and j=1,...,L. A multiplicative random effect term was utilized as the variability in the response for all curves clearly begins at zero, and increases with progressive loading. As already indicated, in the present application, the  $\beta$  term in Eq. (21) can be interpreted as accounting for variability in the anisotropic response of a given sample, and  $\xi$  accounting for the remaining variability.

Eq. (21) can be rewritten for an individual sample response as

$$\begin{bmatrix} \mathbf{s}_{ai}^E \\ \mathbf{s}_{ii}^E \end{bmatrix} = \beta_i \begin{bmatrix} \mathbf{s}_{ai}^M(\boldsymbol{\theta}) \\ \mathbf{s}_{ii}^M(\boldsymbol{\theta}) \end{bmatrix} + \boldsymbol{\xi}$$
 (22)

Due to the normality assumption, the random effects and stochastic error,  $\xi$ , can be integrated out from the model, leaving the likelihood for the data as

$$P\left(s^{E}\middle|\boldsymbol{\theta},\sigma_{\beta}^{2},\sigma_{\xi}^{2}\right) = \frac{1}{(2\pi)^{2LK}\sqrt{|\boldsymbol{\Sigma}|}} \exp\left[\left(s^{E}-s^{M}(\boldsymbol{\theta})\right)^{T} \boldsymbol{\Sigma}^{-1}\left(s^{E}-s^{M}(\boldsymbol{\theta})\right)\right]$$
(23)

with L and K being the number of points used in the discretization of the experimental curves and the number of experimental runs to be evaluated, respectively. The structure of the covariance matrix could be determined from Eqs. (21) and (22), resulting in

$$\Sigma = \mathbb{E}\left[s^{E} s^{E^{T}}\right] - \mathbb{E}\left[s^{E}\right] \mathbb{E}\left[s^{E}\right]^{T} = s^{M} s^{M^{T}} \odot \left(\sigma_{\beta}^{2} I_{K} \otimes J_{2L}\right) + \sigma_{\xi}^{2} I_{2LK}$$
 (24)

where I denotes the identity matrix and J a matrix of ones (subscripts denote their dimension),  $\odot$  the Hadamard product, and  $\otimes$  the Kronecker product. Further details regarding the derivation of Eq. (24) from Eq. (21) can be found in Appendix A.

Utilizing the nomenclature introduced above, Bayes' theorem can be expressed for our application as

$$P\left(\boldsymbol{\theta}, \sigma_{\beta}^{2}, \sigma_{\xi}^{2} \middle| \mathbf{s}^{E}\right) \propto P\left(\mathbf{s}^{E} \middle| \boldsymbol{\theta}, \sigma_{\beta}^{2}, \sigma_{\xi}^{2}\right) P(\boldsymbol{\theta}) P\left(\sigma_{\beta}^{2}, \sigma_{\xi}^{2}\right) \tag{25}$$

Due to a lack of prior knowledge on the damage parameter set, an uninformative uniform prior distribution,  $P(\theta)$  was used in this work. These priors are summarized in Table 2. The elastic moduli bounds were informed by the work of Jefferson et al. (2018). Informative priors were placed on the variance  $\sigma_\xi^2 \sim \text{Ga}(0.01,0.01)$  to encapsulate prior knowledge of minor variability in each individual response curve. Separate variances for  $\beta$  and  $\xi$  in tension and torsion,  $\{\sigma_{\beta\alpha}^2, \sigma_{\beta t}^2, \sigma_{\xi t}^2, \sigma_{\xi t}^2\}$  were also considered with trivial adjustments to the covariance structure in Eq. (24).

## 4.2. Estimation of posterior distribution

The Affine-Invariant MCMC algorithm as described in Section 2.2.1 was used to establish the posterior distribution of the complete set of the model parameters, random effect variances, and stochastic noise variances for the 15-dimensional parameter vector

$$\boldsymbol{\theta} = \left[ E_1, G_{12}, n_{16}, X_{T1}, c_1, q_1, H_{11}, X_{T6}, c_6, q_6, H_{66}, \sigma_{\beta a}^2, \sigma_{\beta t}^2, \sigma_{\xi t}^2, \sigma_{\xi t}^2 \right]^T$$
 (26)

It was estimated using 200 walkers and sampling over 400,000 iterations with an acceptance rate of  $\sim\!17\%$ . Initialization of the ensemble walker positions was established through optimization of the maximum likelihood estimate (MLE) and stochastically placing their positions in a cluster surrounding it. The MLE was found through use of the Nelder-Mead (Nelder and Mead, 1965) method to minimize the negative log-likelihood as the external call to the UMAT represents a 'black-box' function call.

Convergence of MCMC sampling was informed through evolution of the estimated integrated autocorrelation time and mean parameter values in trace plots across all of the chains. Evaluation of the integrated autocorrelation time consisted of evaluation at which point  $\hat{\tau} < N/50$ , alongside the stabilization of this estimate with progressive sampling. The estimated mean integrated autocorrelation time at the end of sampling was found to correspond to roughly 1,700 iterations. With the complete length of the chains, the mean estimate was beginning to asymptotically approach its stable value. In order to minimize the error in the posterior estimate, a burn-in period of 200,000 iterations was removed and the remaining portion of the chain kept as the final result. Fig. 2 shows the mean  $\hat{\tau}$  estimate with increasing number of samples, alongside the trace plots for each parameter considered. Qualitatively, it can be observed that the mean of all walkers stabilizes by 40,000 steps. In Fig. 2a, the evolution of the integrated autocorrelation time is evident along with its asymptotic behavior, along with a trace plot in Fig. 2b further demonstrating the stability of sampling past the burn in period of 200,000 iterations.

The sampled 200 chains were then thinned by a factor of  $0.5\hat{\tau}$  and stacked together. The resulting thinned chain can be visualized in a scatter plot matrix displaying the final 15-dimensional posterior along

**Table 2**Bounds of the uniform priors used in this work for the different damage model parameters.

Parameter	Min.	Max.	
E <sub>1</sub> (GPa)	40	95	
G <sub>12</sub> (GPa)	15	45	
$n_{16}$	0	5	
$X_{T1}$ (MPa)	0	50	
$c_1$	0	100	
$q_1$	0	5	
$H_1$	0	500,000	
X <sub>T6</sub> (MPa)	0	15	
c <sub>6</sub>	0	100	
$q_6$	0	5	
$H_{66}$	0	100,000	

with the marginalized distributions on the main diagonal in Fig. 3. The marginal distributions upon first inspection intuitively display a degree of certainty regarding each model parameter, while correlations between parameters can be observed looking at the off-diagonal. Highly skewed projected distributions such as that between  $\{X_{T6}, c_6\}$  were also readily resolved by the Affine-Invariant MCMC algorithm. From closer inspection of Fig. 3, it can be observed that all marginal distributions were identified with the exception of that for parameter  $H_{11}$ , where the tail was not entirely captured by the assumed prior in Table 2. The prior considered was informed by similar mechanical models, calibrated in a deterministic fashion visually or through least-squares, where it was considered that values exceeding these bounds would be erroneous (Chaboche, 1993; Chaboche et al., 1998; Laurin et al., 2007; Marcin et al., 2011). The obtained posterior, clearly reflects the lack of information contained within the experimental dataset on informing this model parameter. Given the challenges in identifiability of this parameter, evidenced by the truncated tail in the marginal distribution, we believe little additional valuable information would be obtained through expansion of this prior. The contributions of individual experimental tension-torsion specimens on the resulting posterior distribution can be parsed out through performing sequential Bayesian update steps, identifying a distinct posterior distribution at each step. Changes in the posterior distribution at each step can be quantified through various divergence measures, such as the KL-divergence or  $\alpha$ -divergence among many others (Minka, 2005). In this work, all experimental data was used in inferring model parameters.

Summary statistics of the marginal distributions are listed in Table 3 along with the maximum a posteriori (MAP) vector. Evaluation of the statistical model parameter variances demonstrates a higher intersample variability than intra-sample in the response in tension and in torsion. This can more clearly be observed through comparison of the MAP variances corresponding to  $\beta$  and  $\xi$ , and scaling  $\sigma_{\beta a}$  and  $\sigma_{\beta t}$  by the mean of the final stress values across all samples in tension and torsion,  $\overline{s}_{a[-1]}^{M}$  and  $\overline{s}_{t[-1]}^{M}$ , respectively. This process results in ratios of  $ar{s}_{a[-1]}^{M}\sigma_{eta a} / \sigma_{\xi a} pprox 25.067$  and  $ar{s}_{t[-1]}^{M}\sigma_{eta t} / \sigma_{\xi t} pprox 1.813$ . This simple postprocessing check highlights the importance of considering intersample variability in the governing statistical model when evaluating inhomogeneous experimental datasets, particularly on composite materials where a high level of variability in the anisotropic response is expected. Through further inspection of the moments of the distributions in Table 3, it can be seen that none of the marginal distributions of damage model parameters could be simply approximated as Gaussian. The marginalized distribution characteristics for each model parameter can be interpreted in terms of the relative uncertainty of the model conditioned on the observed dataset. The parameters  $E_1$ ,  $G_{12}$ ,  $c_6$ , and  $g_6$ all exhibited coefficients of variation (CV) below 10% identifying tight clustering around the mean and a relative degree of certainty regarding the underlying value. Higher order moments of these distributions (skewness and kurtosis), with the exception of  $G_{12}$ , are all positive and approximately zero, signifying minimal positive skew to each distribution, and normalized kurtosis values identifying each as a leptokurtic distribution.  $G_{12}$  is equivalently identified as a platykurtic distribution with negative skew. Parameters exhibiting large deviations from Gaussian are  $X_{T1}$ ,  $n_{16}$ , and  $q_1$ , all of which are significantly positively skewed with excess kurtosis values signifying larger tails and a higher likelihood of outliers. Not surprisingly, these insights are also observed in the CV values reported for these parameters, where each has values in excess of 30%, with a peak value of approximately 102% for  $X_{T1}$ . Returning to Fig. 3 to further evaluate  $X_{T1}$ , the heavy skew of the marginalized distribution becomes evident on the main diagonal. While the mode is clearly identified, the overall uncertainty of this parameter remains high with a standard deviation  $\sim$ 7× the MAP value. This uncertainty in initial strength  $(X_{T1})$  of the material in damage mode 1 should not be unexpected when looking at the experimental response curves in Fig. 1. All of the curves in tension (and the singular test in

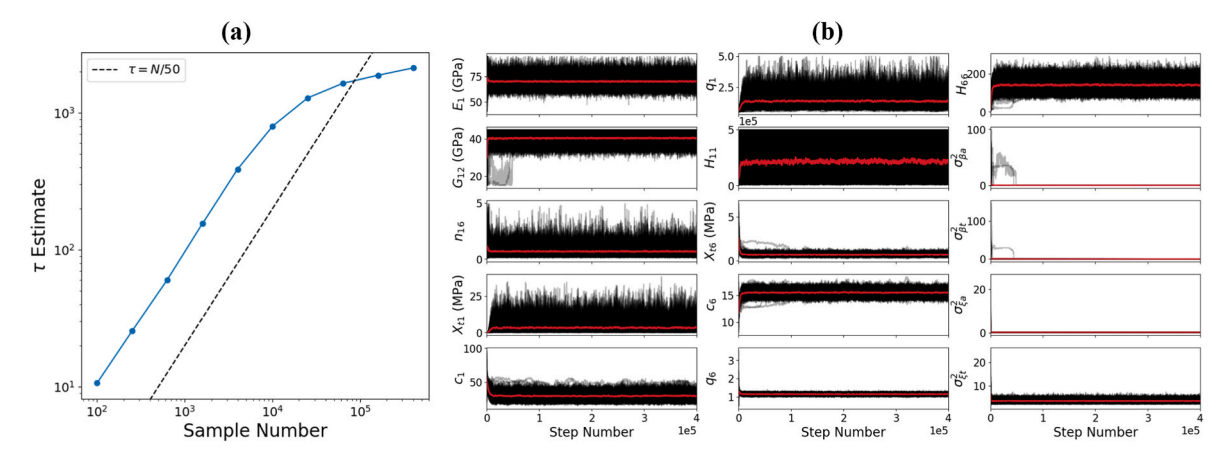


Fig. 2. (a) Plot of estimated mean integrated autocorrelation time across all chains with increasing total chain length. (b) Trace plots for all parameter values with overlaid traces for each walker shown against increasing step number with the mean of all walkers displayed in red.

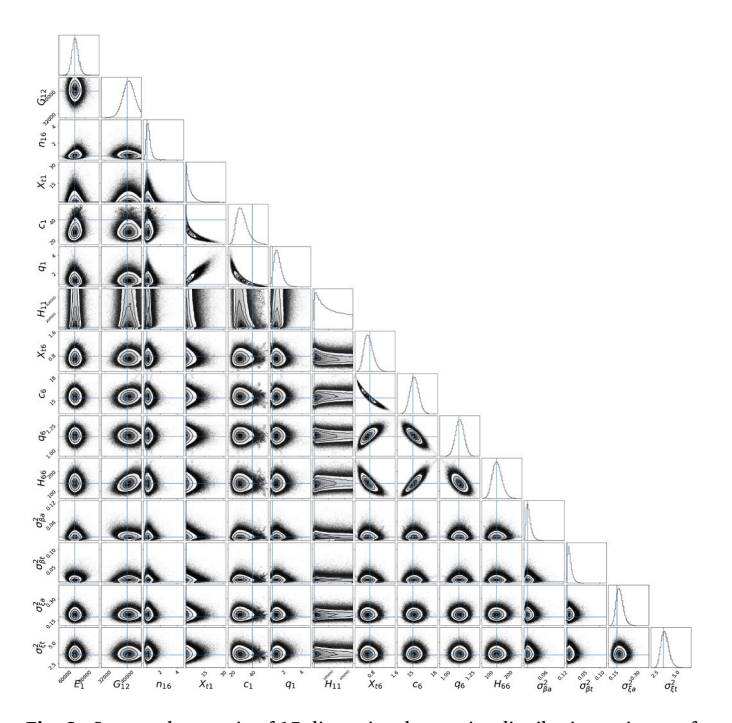


Fig. 3. Scatter plot matrix of 15-dimensional posterior distribution estimate of viscous multimode damage model and noise parameters, with the maximum a posteriori (MAP) value highlighted in blue. Contours denote the  $0.5\sigma$ ,  $1.0\sigma$ ,  $1.5\sigma$ , and  $2.0\sigma$  confidence intervals. Plotting utilized a package in Python by Foreman-Mackey (Foreman-Mackey, 2016).

compression) exhibit little nonlinear behavior prior to failure, in direct contrast to the material response in torsion. This response presents challenges in the identification of model parameters  $X_{T1}$ ,  $c_1$ , and  $q_1$ . Adjustment of these three parameters simultaneously permits wide ranging values of each in their marginalized distributions to match the approximately linear elastic behavior observed in tension.  $X_{T1}$ , denoting the onset of damage establishes the initial threshold energy release rate,  $y_{\alpha}^0$ , in Eq. (3). The growth rate in the energy release rate threshold  $y_{\alpha}$  (which encompasses viscous effects) for further damage accumulation is then controlled with the constant  $c_1$  (see Eq. (3)). Finally, the power law form of the damage accumulation rate expression (see Eq. (11)) is influenced by the exponent  $q_1$ . Modulation of all three of these parameters can control the onset of damage with  $X_{T1}$  as well as the overall rate of damage accumulation directly through  $q_1$  and indirectly through  $c_1$ . This is further borne out in the projected joints (indexed by (5,4), (6,4),

and (6,5)) in Fig. 3 demonstrating a high level of mutual information between the identified damage variables.

The posterior distribution was then sampled, passed through the mechanical model and displayed against the experimental curves upon which the parameters were conditioned. Plots of this result along with the MAP vector and 1,000 samples can be seen in Fig. 4 for each loading case.

The resulting curves drawn from the posterior display different levels of discrepancies between the model predictions and the experimentally observed stress-strain curves. Following the discussion and model of Kennedy O'Hagan (Kennedy and O'Hagan, 2001), this discrepancy can be broken into: (i) stochastic error induced by the measurement apparatus, (ii) error owing to the variability in the involute tube layup and resulting mechanical properties, and (iv) the error attributed to limitations in the mechanical model formulation. From the preceding sections, it should be apparent that the first two sources of error were accounted for through the model presented in Eq. (21). While the model discrepancy term was clearly non-negligible from Fig. 4, its inclusion in the Kennedy O'Hagan model was omitted as the goal of this work was to probabilistically calibrate the present damage model rather than evaluate its predictive capability. Inclusion of discrepancy modeling is left as an avenue of future research in the Bayesian treatment of complex multimodal mechanical models.

## 4.3. Identification of subsequent experimental tests

Of particular interest in the characterization of materials is the ability of this Bayesian workflow to provide valuable information on subsequent experimental tests which maximize the potential information gain. In traditional model calibration, often there is an available dataset of varying degrees of quality, which is utilized to identify a deterministic parameter set minimizing an error metric between model predictions and experimental observations. The Bayesian workflow demonstrated in this work, and identified mechanical model parameter posterior distribution in Fig. 3, can facilitate an active learning approach for the subsequent selection of testing conditions which would maximize the constitutive model accuracy across a domain of interest. Examples of such active learning approaches include, uncertainty sampling (Lewis and Catlett, 1994) and entropy-based selection (Herbrich et al., 2003), where new test conditions are identified based on the largest posterior variance, along with selection by maximum difference from current estimates (Wang and Li, 2018), or selection by maximum expected improvement in the model fit (Yue et al., 2020), or batch selection according to distance in the input (Loeppky et al., 2010), among many others (Ginsbourger, 2018; Yue et al., 2020). As a demonstration of the above procedure in the current work, an input domain of tensile

Table 3
Statistical measures of marginalized posterior distributions including the MAP, mean, standard deviation, skewness, kurtosis, and coefficient of variation.

$\theta$	MAP	Mean	Std. Dev.	Skew.	Kurt.	CV (%)
E <sub>1</sub> (GPa)	69.579	70.147	3.410	0.336	1.032	4.862
$G_{12}$ (GPa)	39.995	40.447	2.048	-0.194	-0.132	5.064
$n_{16}$	0.500	0.681	0.276	1.598	5.557	40.558
$X_{T1}$ (MPa)	0.444	3.263	3.314	1.947	5.150	101.558
$c_1$	39.724	29.718	5.764	0.907	1.053	19.397
$q_1$	0.751	1.361	0.455	1.148	2.576	33.458
$H_{11}$	2.641E+04	2.160E+05	1.422E+05	0.351	-1.117	65.816
$X_{T6}$ (MPa)	0.742	0.703	0.155	0.499	0.302	22.093
c <sub>6</sub>	15.292	15.482	0.557	0.167	0.077	3.595
$q_6$	1.134	1.142	0.043	0.028	0.056	3.791
$H_{66}$	138.108	141.086	24.594	0.356	0.234	17.432
$\sigma_{eta a}^2$	0.014	0.129	0.030	0.765	0.887	23.155
$\sigma_{eta t}^2$	0.005	0.110	0.028	0.858	1.116	25.849
$\sigma_{\xi a}^2$	0.173	0.438	0.028	0.322	0.194	6.304
$\sigma_{\xi t}^2$	3.517	1.919	0.120	0.306	0.171	6.276

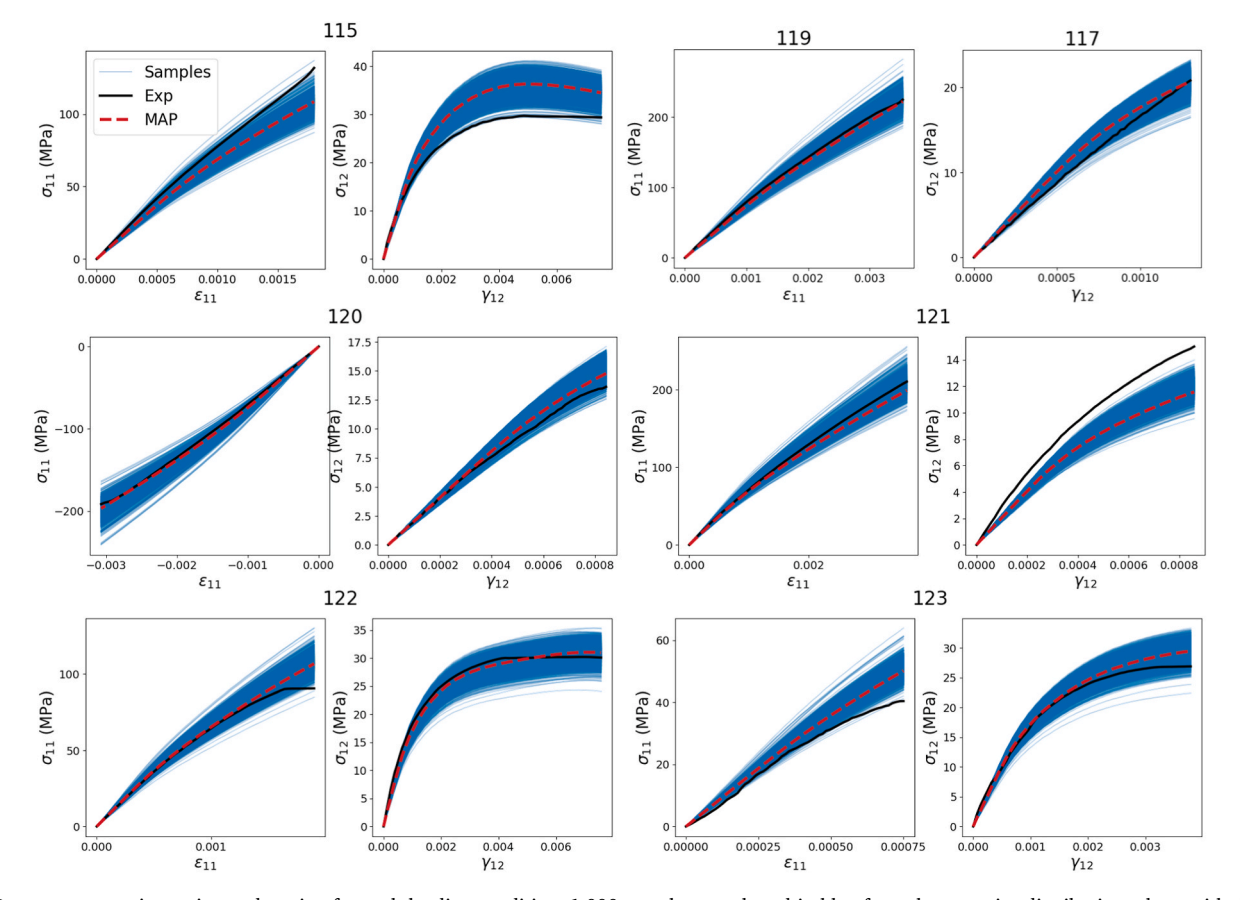


Fig. 4. Response curves in tension and torsion for each loading condition. 1,000 samples are plotted in blue from the posterior distribution, along with the curve resulting from the MAP vector in red and the experimentally observed response in black.

multiaxial strain rates  $\{\dot{\epsilon}_{11},\dot{\gamma}_{12}\}$  was discretized into 100 bins, and the posterior was passed through the forward mechanical model, with corresponding effective loading rates determined from the mechanical model output. At each location in the input domain, the mean variance of the posterior predictions across the multiaxial response curves was evaluated, with the topology of the resulting variance map displayed in Fig. 5.

The candidate experimental test condition exhibiting the maximum predicted variance is then selected as the next experiment to be run. This cycle of populating variance values on the input domain, and maximum selection is repeated as many times as needed – usually until the model results in error stabilization across the accumulated experimental

dataset. In the current case, a map of the posterior propagated variance across the input domain can be observed in Fig. 5, with the peak uncertainty present at the test conditions of  $\dot{\sigma}_{11}=0.47$  and  $\dot{\sigma}_{12}=0.40$  in MPa/s, informing the subsequent experimental run.

### 5. Conclusions

The work described in this paper significantly advances Bayesian methods as applied to material constitutive model development. It provides several advantages over prior work: (i) it demonstrates the feasibility of simultaneous calibration over inhomogeneous datasets with multiaxial loading, facilitated through the use a statistical model

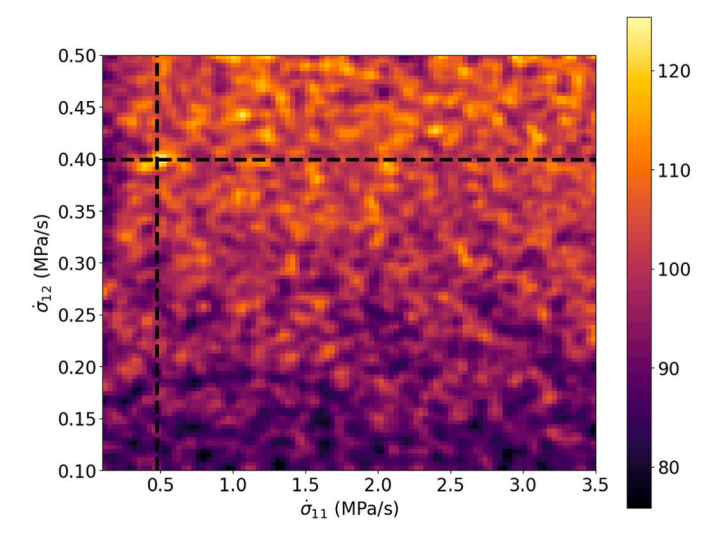


**Fig. 5.** Map of predicted mean variance across multiaxial tensile response. Predicted variances were identified by passing the identified posterior distribution on model parameters through the mechanical model at each combination in the strain rate input space. Maximum variance location is highlighted at  $\dot{\sigma}_{11}=0.47$  and  $\dot{\sigma}_{12}=0.40$  MPa/s.

accounting for inter-sample variability, (ii) allows for modular incorporation of the widely used Abaqus UMATs for material development, (iii) extends probabilistic calibration from simple mechanics models to CDM models with large quantities of unknown parameters corresponding to elastic constants, coupling and evolution functions, and (iv) delivers a workflow for the objective and rigorous quantification of uncertainty in stochastic material model parameters. Overall, this work enables the probabilistic calibration of complex constitutive models when provided with sparse and inhomogeneous datasets. A limitation of this work presented exists in the omission of a statistical quantification of the model discrepancy, or inability to perfectly capture the underlying physics. This additional activity is left as an avenue of future research to

better quantify performance of CDM models. The end result of this work provides a promising approach for the probabilistic calibration of complex high-dimensional material models.

## Authorship statement

Conception of design of study: Adam P. Generale, Surya R. Kalidindi, Richard B. Hall, Robert A. Brockman. Acquisition of experimental data: George Jefferson, Larry Zawada, Jennifer Pierce. Analysis and interpretation of data: Adam P. Generale, V. Roshan, Joseph, Surya R. Kalidindi, Robert A. Brockman, George Jefferson, Richard B. Hall, Jennifer Pierce. Drafting of manuscript: Adam P. Generale, Surya R. Kalidindi, Richard B. Hall, Robert A. Brockman. Revising manuscript: Adam P. Generale, Surya R. Kalidindi, V. Roshan, Joseph, Richard B. Hall, Robert A. Brockman. Approval of the version of manuscript to be published: Adam P. Generale, Surya R. Kalidindi, V. Roshan, Joseph, Richard B. Hall, Robert A. Brockman.

## Declaration of competing interest

The authors declare that they have no known competing financial interests or personal relationships that could have appeared to influence the work reported in this paper.

## Data availability

The authors do not have permission to share data.

#### Acknowledgements

This research was sponsored by the Department of Defense (DoD) High Performance Computing Modernization Program (HPCMP) 2020 HPC Internship Program (HIP) and the National Science Foundation award 2027105. This work utilized computing resources supported by Air Force Research Laboratory (AFRL).

# Appendix A

The details of establishing the covariance matrix in Eq. (24) are presented in this section. The derivation starts with the classical definition of the covariance matrix, utilizing the flattened structure of  $s^E$  previously presented in Eq. (20) as

$$\mathbf{\Sigma} = \mathbb{E}\left[\mathbf{s}^{E}\mathbf{s}^{E^{T}}\right] - \mathbb{E}\left[\mathbf{s}^{E}\right]\mathbb{E}\left[\mathbf{s}^{E}\right]^{T} \tag{A.1}$$

In this vectorized notation, Eq. (21) can be rewritten as

$$s^{E} = \beta \otimes 1_{2L} \odot s^{M} + \xi \tag{A.2}$$

where  $\mathbf{1}_{2L}$  denotes a vector of ones with length 2L,  $\boldsymbol{\beta}$  a random vector  $\boldsymbol{\beta} = [\boldsymbol{\beta}_1, ..., \boldsymbol{\beta}_K]^T$ ,  $s^M$  a vector of model output stresses matching to the structure of  $s^E$  with length 2LK, and  $\boldsymbol{\xi}$  a random vector of Gaussian white noise, similarly with dimension 2LK. Substitution of  $s^E$  into Eq. (A.2) along with further simplification leads to

$$\Sigma = \mathbb{E}\Big[ (\boldsymbol{\beta} \otimes \mathbf{1}_{2L} \odot s^{M} + \boldsymbol{\xi}) (\boldsymbol{\beta} \otimes \mathbf{1}_{2L} \odot s^{M} + \boldsymbol{\xi})^{T} \Big] - \mathbb{E}[\boldsymbol{\beta} \otimes \mathbf{1}_{2L} \odot s^{M} + \boldsymbol{\xi}] \mathbb{E}[\boldsymbol{\beta} \otimes \mathbf{1}_{2L} \odot s^{M} + \boldsymbol{\xi}]^{T} = \mathbb{E}\Big[ s^{M} s^{M^{T}} \odot (\boldsymbol{\beta} \otimes \mathbf{1}_{2L}) (\boldsymbol{\beta} \otimes \mathbf{1}_{2L})^{T} \Big] + \sigma_{\xi}^{2} I_{2LK} - s^{M} s^{M^{T}}$$

$$= s^{M} s^{M^{T}} \odot \mathbb{E}[\boldsymbol{\beta} \boldsymbol{\beta}^{T} \otimes \boldsymbol{J}_{2L}] + \sigma_{\xi}^{2} I_{2LK}$$
(A.3)

At this point, through noting independence of  $\beta_i \sim N(1, \sigma_{\beta}^2)$ , the final covariance structure of Eq. (24) can be obtained, which is repeated in Eq. (A.4).

$$\mathbf{\Sigma} = \mathbf{s}^{M} \mathbf{s}^{M^{T}} \odot \left( \sigma_{\beta}^{2} \mathbf{I}_{K} \otimes \mathbf{J}_{2L} \right) + \sigma_{\varepsilon}^{2} \mathbf{I}_{2LK} \tag{A.4}$$

This covariance matrix can be adjusted to introduce independence between the multiplicative random effect in tension and torsion through adjusting both  $s^E$  and  $s^M$  to order all stress values in tension, followed by all stress values in torsion as

$$\mathbf{s}^{E} = \begin{bmatrix} \mathbf{s}_{a1}^{T} & \cdots & \mathbf{s}_{aK}^{T} & \mathbf{s}_{t1}^{T} & \cdots & \mathbf{s}_{tK}^{T} \end{bmatrix}^{T}$$
(A.5)

with  $s^M$  following accordingly. Separate distributions for  $\beta_{ia} \sim N(1, \sigma_{\beta a}^2)$  and  $\beta_{it} \sim N(1, \sigma_{\beta t}^2)$  can now be incorporated resulting in the expression found in Eq. (A.6).

$$\mathbf{M}_{\beta} = \begin{bmatrix} \sigma_{\beta a}^2 & 0 \\ 0 & \sigma_{\beta t}^2 \end{bmatrix}$$

$$\mathbf{\Sigma} = \mathbf{s}^M \mathbf{s}^{M^T} \odot (\mathbf{M}_{\beta} \otimes \mathbf{I}_K \otimes \mathbf{J}_L) + \sigma_t^2 \mathbf{I}_{2JK}$$
(A.6)

#### References

- Adeli, E., Matthies, H.G., 2019. Parameter Identification in Viscoplasticity Using Transitional Markov Chain Monte Carlo Method arXiv:1906.10647 [cs].
- Adeli, E., Rosić, B., Matthies, H.G., Reinstädler, S., Dinkler, D., 2020. Comparison of Bayesian methods on parameter identification for a viscoplastic model with damage. Metals 10, 876. https://doi.org/10.3390/met10070876.
- Bansal, N.P., Lamon, J. (Eds.), 2014. Ceramic Matrix Composites: Materials, Modeling and Technology. John Wiley & Sons, Inc., Hoboken, NJ, USA https://doi.org/ 10.1002/9781118832998.
- Belytschko, T., Liu Kam, W., Moran, B., Elkhodary, K., 2014. Nonlinear Finite Elements for Continua and Structures, second ed. John Wiley & Sons, Inc.
- Box, G.E.P., Hunter, W.G., 1962. A useful method for model-building. Technometrics 4, 301–318. https://doi.org/10.1080/00401706.1962.10490015.
- Camus, G., 2000. Modelling of the mechanical behavior and damage processes of fibrous ceramic matrix composites: application to a 2-D SiC/SiC. Int. J. Solid Struct. 37, 919–942. https://doi.org/10.1016/S0020-7683(99)00065-7.
- Castillo, A., Kalidindi, S.R., 2019. A Bayesian framework for the estimation of the single crystal elastic parameters from spherical indentation stress-strain measurements. Front. Mater. 6, 136. https://doi.org/10.3389/fmats.2019.00136.
- Chaboche, J.-L., 1993. Development of continuum damage mechanics for elastic solids sustaining anisotropic and unilateral damage. Int. J. Damage Mech. 2, 311–329. https://doi.org/10.1177/105678959300200401.
- Chaboche, J.L., Lesné, O., Pottier, T., 1998. Continuum damage mechanics of composites: towards a unified approach. In: Studies in Applied Mechanics. Elsevier, pp. 3–26. https://doi.org/10.1016/S0922-5382(98)80032-9.
- Chaboche, J.-L., Maire, J.-F., 2002. A new micromechanics based CDM model and its application to CMC's. Aero. Sci. Technol. 6, 131–145. https://doi.org/10.1016/ \$1270.9638(02)01154-9
- Chontos, A., Huber, D., Berger, T.A., Kjeldsen, H., Serenelli, A.M., Aguirre, V.S., Ball, W. H., Basu, S., Bedding, T.R., Chaplin, W.J., Claytor, Z.R., Corsaro, E., Garcia, R.A., Howell, S.B., Lundkvist, M.S., Mathur, S., Metcalfe, T.S., Nielsen, M.B., Ong, J.M.J., Orhan, Z.Ç., Örtel, S., Salama, M., Stassun, K.G., Townsend, R.H.D., Saders, J.L. van, Winther, M., Yildiz, M., Butler, R.P., Tinney, C.G., Wittenmyer, R.A., 2021. TESS asteroseismology of alpha mensae: benchmark ages for a G7 Dwarf and its M Dwarf companion. ApJ 922, 229. https://doi.org/10.3847/1538-4357/ac1269.
- Dassault, S., 2019. Abaqus/CAE User's Manual 1174.
- Davidian, M., Giltinan, D.M., 2003. Nonlinear models for repeated measurement data: an overview and update. JABES 8, 387–419. https://doi.org/10.1198/1085711032697.
- Davidian, M., Giltinan, D.M., 1993. Analysis of repeated measurement data using the nonlinear mixed effects model. Chemometr. Intell. Lab. Syst. 20, 1–24. https://doi. org/10.1016/0169-7439(93)80017-C.
- DeRienzo, J.M., 2013. Bi-Axial (Tension-Torsion) Testing of an Oxide/Oxide Ceramic Matrix Composite. Air Force Institute of Technology.
- Ding, J., Wang, Y.D., Gulzar, S., Kim, Y.R., Underwood, B.S., 2020. Uncertainty quantification of simplified viscoelastic continuum damage fatigue model using the Bayesian inference-based Markov chain Monte Carlo method. Transport. Res. Rec. 2674, 247–260. https://doi.org/10.1177/0361198120910149.
- Foreman-Mackey, D., 2021. Autocorrelation Analysis & Convergence emcee [WWW Document]. URL. https://emcee.readthedocs.io/en/stable/tutorials/autocorr/ (Accessed 21 October 2021).
- Foreman-Mackey, D., 2016. corner.py: scatterplot matrices in Python. J. Open Source Softw. 1, 24. https://doi.org/10.21105/joss.00024.
- Foreman-Mackey, D., Hogg, D.W., Lang, D., Goodman, J., 2013. emcee: the MCMC Hammer, vol. 125. Publications of the Astronomical Society of the Pacific, pp. 306–312. https://doi.org/10.1086/670067.
- Gallina, A., Ambrozinski, L., Pieczonka, P., Uhl, T., Staszewski, W., 2015. Bayesian parameter identification of orthotropic composite materials using lamb waves dispersion curves measurement - Alberto Gallina, Lukasz Ambrozinski, Pawel Packo, Lukasz Pieczonka, Tadeusz Uhl, Wieslaw J Staszewski. J. Vib. Control 23, 2017.
- Ginsbourger, D., 2018. Sequential design of computer experiments. In: Balakrishnan, N., Colton, T., Everitt, B., Piegorsch, W., Ruggeri, F., Teugels, J.L. (Eds.), Wiley StatsRef: Statistics Reference Online. John Wiley & Sons, Ltd, Chichester, UK, pp. 1–9. https://doi.org/10.1002/9781118445112.stat08124.
- Goodman, J., Weare, J., 2010. Ensemble samplers with affine invariance. CAMCoS 5, 65–80. https://doi.org/10.2140/camcos.2010.5.65.
- Hall, R., Apostolov, Z., Hilmas, A., Jefferson, G., Varshney, V., Cinibulk, M., Brockman, R., Hoffman, R., Key, T., King, D., 2021. Evolutive state and damage modeling and characterization for PIP-based high-speed vehicle materials. In: Presented at the MS&T21. Materials Science & Technology Technical Meeting and Exhibition, Columbus, OH.

- Hall, R., Brockman, R., 2020. Viscoelastoplastic oxidative multimode damage model for fibrous composite materials at extreme temperatures. In: Presented at the Society for Experimental Mechanics, Virtual Annual Conference and Exposition on Experimental and Applied Mechanics and XIV International Congress.
- Hall, R.B., Brockman, R.A., 2021. Viscoelastoplastic oxidative multimode damage model for fibrous composite materials at extreme temperatures. In: Silberstein, M., Amirkhizi, A. (Eds.), Challenges in Mechanics of Time Dependent Materials, ume 2. Springer International Publishing, Cham, pp. 55–58. https://doi.org/10.1007/978-3-030-59542-5 9.
- Hall, R.B., Brockman, R.A., Generale, A.P., Joseph, V.R., Kalidindi, S.R., 2022. A viscous damage theory for ceramic matrix composites in multi-axial loading. In: Proceedings of the 12th International Conference on the Mechanics of Time Dependent Materials. Dallas. TX.
- Herbrich, R., Lawrence, N.D., Seeger, M., 2003. Fast sparse Gaussian process methods: the informative vector machine. In: Becker, S., Thrun, S., Obermayer, K. (Eds.), Advances in Neural Information Processing Systems 15. MIT Press, pp. 625–632.
- Hilburn, S.R., 2014. Experimental Investigation of Mechanical Behavior of an Oxide/ Oxide Ceramic Matrix Composite in Interlaminar Shear and under Combined Tension-Torsion. Air Force Institute of Technology.
- Hogg, D.W., Foreman-Mackey, D., 2018. Data analysis recipes: using Markov chain Monte Carlo. ApJS 236, 11. https://doi.org/10.3847/1538-4365/aab76e.
- Huang, S., Yin, H., Hu, S., Chen, X., Jiang, Y., Alexeeva, S., Wang, Y., 2021. The X-ray outburst of PG 1553\$\text{mathplus\$113:} a precession effect of two jets in the supermassive black hole binary system. APJ (Acta Pathol. Jpn.) 922, 222. https://doi.org/10.3847/1538-4357/ac2d98.
- Jefferson, G., Zawada, L., Pierce, J., Jones, E., Przybyla, C., 2018. Multi-axial Failure Characterization of Oxide-Oxide CMC's. Presented at the Materials Science & Technology (MS&T) Conference, Columbus, OH.
- Kachanov, L., 1986. Introduction to Continuum Damage Mechanics, Mechanics of Elastic Stability. Springer Netherlands. https://doi.org/10.1007/978-94-017-1957-5.
- Kennedy, M.C., O'Hagan, A., 2001. Bayesian calibration of computer models. J. Roy. Stat. Soc. B (Stat. Methodol.) 63, 425–464. https://doi.org/10.1111/1467-9868.00294.
- Kirsch, A., 2011. An Introduction to the Mathematical Theory of Inverse Problems, Applied Mathematical Sciences. Springer, New York, NY. https://doi.org/10.1007/ 978-1-4419-8474-6 5.
- Knipprath, C., 2010. Mechanical Performance of Binder Yarn Composites. Cranfield University.
- Kumar, R.S., Mordasky, M., Ojard, G., Yuan, Z., Fish, J., 2019. Notch-strength prediction of ceramic matrix composites using multi-scale continuum damage model. Materialia 6, 100267. https://doi.org/10.1016/j.mtla.2019.100267.
- Laurin, F., Carrère, N., Maire, J.-F., 2007. A multiscale progressive failure approach for composite laminates based on thermodynamical viscoelastic and damage models. Compos. A Appl. Sci. Manuf. 38, 198–209. https://doi.org/10.1016/j. compositesa.2006.01.018.
- Lemaitre, J., 1992. A Course on Damage Mechanics. Springer-Verlag, Berlin Heidelberg. https://doi.org/10.1007/978-3-662-02761-5.
- Lemaitre, J., 1984. How to use damage mechanics. Nucl. Eng. Des. 233–245. https://doi. org/10.1016/0029-5493(84)90169-9, 4th Special Issue on Smirt-7 80.
- Lemaitre, J., Chaboche, J.-L., 1990. Mechanics of Solid Materials. Cambridge University Press, Cambridge. https://doi.org/10.1017/CBO9781139167970.
- Lewis, D.D., Catlett, J., 1994. Heterogeneous uncertainty sampling for supervised learning. In: Cohen, W.W., Hirsh, H. (Eds.), Machine Learning Proceedings 1994. Morgan Kaufmann, San Francisco (CA), pp. 148–156. https://doi.org/10.1016/
- Loeppky, J.L., Moore, L.M., Williams, B.J., 2010. Batch sequential designs for computer experiments. J. Stat. Plann. Inference 140, 1452–1464. https://doi.org/10.1016/j.ispi 2009 12 004
- Mahnken, R., 2017. Identification of material parameters for constitutive Equations. In: Encyclopedia of Computational Mechanics, second ed. American Cancer Society, pp. 1–21. https://doi.org/10.1002/9781119176817.ecm2043.
- Marcin, L., Maire, J.-F., Carrère, N., Martin, E., 2011. Development of a macroscopic damage model for woven ceramic matrix composites. Int. J. Damage Mech. 20, 939–957. https://doi.org/10.1177/1056789510385259.
- Matzenmiller, A., Lubliner, J., Taylor, R.L., 1995. A constitutive model for anisotropic damage in fiber-composites. Mech. Mater. 20, 125–152. https://doi.org/10.1016/0167-6636(94)00053-0.
- Mehrez, L., Kassem, E., Masad, E., Little, D., 2015. Stochastic identification of linearviscoelastic models of aged and unaged asphalt mixtures. J. Mater. Civ. Eng. 27.
- Miles, P., Hays, M., Smith, R., Oates, W., 2015. Bayesian uncertainty analysis of finite deformation viscoelasticity. Mech. Mater. 91, 35–49. https://doi.org/10.1016/j. mechmat.2015.07.002.

- Minka, T., 2005. Divergence Measures and Message Passing 17.
- Murakami, S., 2012. Continuum Damage Mechanics, Solid Mechanics and its Applications. Springer Netherlands, Dordrecht. https://doi.org/10.1007/978-94-007-2666-6
- Nelder, J.A., Mead, R., 1965. A simplex method for function minimization. Comput. J. 7, 308–313. https://doi.org/10.1093/comjnl/7.4.308.
- Oliver, J., 1989. A consistent characteristic length for smeared cracking models. Int. J. Numer. Methods Eng. 28, 461–474. https://doi.org/10.1002/nme.1620280214.
- Pacheo, C.C., Dulikravich, G.S., Vesenjak, M., Borovinšek, M., Duarte, I.M.A., Jha, R., Reddy, S.R., Orlande, H.R.B., Colaço, M.J., 2016. Inverse parameter identification in solid mechanics using Bayesian statistics, response surfaces and minimization. Techn. Mech. Eur. J. Eng. Mech. 36, 120–131. https://doi.org/10.24352/UB. OVGI-2017-014.
- Pagano, N.J., Whitford, L.E., 1985. On the solution for the elastic response of involute bodies. Compos. Sci. Technol. 22, 295–317. https://doi.org/10.1016/0266-3538 (85)90066-1
- Pailhes, J., Camus, G., Lamon, J., 2002. A constitutive model for the mechanical behavior of a 3D C/C composite. Mech. Mater. 34, 161–177. https://doi.org/10.1016/S0167-6636(01)00101-6.
- Pinheiro, J., Bates, D., Lindstrom, M., 2007. Model Building for Nonlinear Mixed Effects
- Rajagopal, K.R., Srinivasa, A.R., 2004. On thermomechanical restrictions of continua. Proc. R. Soc. Londn. Ser. A: Math. Phys. Eng. Sci. 460, 631–651. https://doi.org/ 10.1098/rspa.2002.1111.
- Rajagopal, K.R., Srinivasa, A.R., 1998. Mechanics of the inelastic behavior of materials. Part II: inelastic response. Int. J. Plast. 14, 969–995. https://doi.org/10.1016/ S0749-6419(98)00041-2.
- Roy, V., 2019. Convergence Diagnostics for Markov Chain Monte Carlo arXiv: 1909.11827 [stat].
- Simo, J.C., Ju, J.W., 1987. Strain- and stress-based continuum damage models—I. Formulation. Int. J. Solid Struct. 23, 821–840. https://doi.org/10.1016/0020-7683 (87)90083-7.

- Sokal, A., 1996. Monte Carlo Methods in Statistical Mechanics: Foundations and New Algorithms Note to the Reader.
- Suárez Mascareño, A., Damasso, M., Lodieu, N., Sozzetti, A., Béjar, V.J.S., Benatti, S., Zapatero Osorio, M.R., Micela, G., Rebolo, R., Desidera, S., Murgas, F., Claudi, R., González Hernández, J.I., Malavolta, L., Burgo, C. del, D'Orazi, V., Amado, P.J., Locci, D., Tabernero, H.M., Marzari, F., Aguado, D.S., Turrini, D., Cardona Guillén, C., Toledo-Padrón, B., Maggio, A., Aceituno, J., Bauer, F.F., Caballero, J.A., Chinchilla, P., Esparza-Borges, E., González-Álvarez, E., Granzer, T., Luque, R., Martín, E.L., Nowak, G., Oshagh, M., Pallé, E., Parviainen, H., Quirrenbach, A., Reiners, A., Ribas, I., Strassmeier, K.G., Weber, M., Mallonn, M., 2021. Rapid contraction of giant planets orbiting the 20-million-year-old star V1298 Tau. Nat. Astron. 1–9. https://doi.org/10.1038/s41550-021-01533-7.
- Van Oijen, M., Rougier, J., Smith, R., 2005. Bayesian calibration of process-based forest models: bridging the gap between models and data. Tree Physiol. 25, 915–927. https://doi.org/10.1093/treephys/25.7.915.
- Wang, H., Li, J., 2018. Adaptive Gaussian process approximation for Bayesian inference with expensive likelihood functions. Neural Comput. 30, 3072–3094. https://doi. org/10.1162/neco a 01127.
- Wu, X., Kozlowski, T., Meidani, H., Shirvan, K., 2018. Inverse uncertainty quantification using the modular Bayesian approach based on Gaussian process, Part 1: Theory. Nucl. Eng. Des. 335, 339–355. https://doi.org/10.1016/j.nucengdes.2018.06.004.
- Yue, X., Wen, Y., Hunt, J.H., Shi, J., 2020. Active learning for Gaussian process considering uncertainties with application to shape control of composite fuselage. IEEE Trans. Autom. Sci. Eng. 1–11. https://doi.org/10.1109/TASE.2020.2990401.
- Zhang, E., Chazot, J.D., Antoni, J., 2012. Parametric identification of elastic modulus of polymeric material in laminated glasses. IFAC Proc. Vol. 45, 422–427. https://doi. org/10.3182/20120711-3-BE-2027.00222.
- Zhang, E., Chazot, J.D., Antoni, J., Hamdi, M., 2013. Bayesian characterization of Young's modulus of viscoelastic materials in laminated structures. J. Sound Vib. 332, 3654–3666. https://doi.org/10.1016/j.jsv.2013.02.032.